ACS Catalysis

Research Article

Cite This: ACS Catal. 2018, 8, 6827−6836

pubs.acs.org/acscatalysis

Graphitic Nitrogen Is Responsible for Oxygen Electroreduction on Nitrogen-Doped Carbons in Alkaline Electrolytes: Insights from Activity Attenuation Studies and Theoretical Calculations

Nan Wang,[†] Bingzhang Lu,[‡] Ligui Li,*[,†,§] Wenhan Niu,[†] Zhenghua Tang,[†,§] Xiongwu Kang,[†] and Shaowei Chen*[,†,‡]

[†]Guangzhou Key Laboratory for Surface Chemistry of Energy Materials, New Energy Research Institute, School of Environment and Energy, South China University of Technology, Guangzhou Higher Education Mega Center, Guangzhou 510006, China

[‡]Department of Chemistry and Biochemistry, University of California, 1156 High Street, Santa Cruz, California 95064, United States

[§]Guangdong Provincial Key Laboratory of Atmospheric Environment and Pollution Control, School of Environment and Energy, South China University of Technology, Guangzhou 510006, China

Supporting Information

ABSTRACT: To date, controversies remain in the unambiguous identification of the active sites in N-doped carbons for oxygen reduction reaction (ORR). In the present study, prolonged potential cycling was conducted on three N-doped carbons in O_2-saturated 0.1 M KOH aqueous solution, where apparent attenuation of the ORR activity was observed, within the context of limiting current and onset potential. The attenuation trend of the limiting current was closely correlated with the diminishing content of graphitic N, as manifested in X-ray photoelectron spectroscopy measurements and Mott−Schottky analysis. In addition, the specific activity per graphitic N was found to be almost invariant within a wide range of potentials during prolonged potential cycling for all three model catalysts, in good agreement with theoretical prediction, whereas no such a correlation was observed with pyrrolic or pyridinic N. Density functional theory calculations showed that the first-electron reduction, which is a rate-determining step for the 4e⁻ ORR process, on carbon atoms adjacent to graphitic N, exhibited a much smaller Gibbs free-energy change than that on carbons neighboring pyrrolic or pyridinic N. These results strongly suggest that graphitic N is responsible for the ORR activity of N-doped carbons in alkaline electrolytes. Results in the present work may offer a generic, effective paradigm in the determination of catalytic active sites in heteroatom-doped carbons and be exploited as a fundamental framework for the rational design and engineering of effective carbon catalysts.

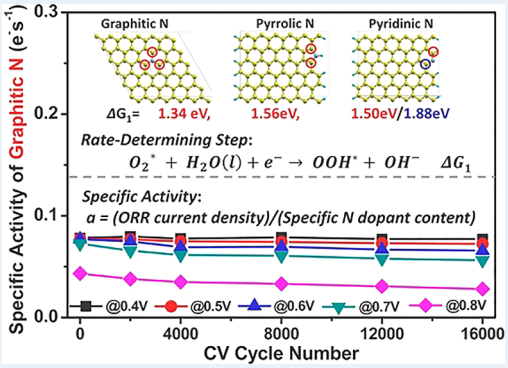

KEYWORDS: *nitrogen-doped carbon, oxygen reduction reaction, activity attenuation, active site, graphitic nitrogen*

INTRODUCTION

Nitrogen-doped carbons have emerged as a promising, low-cost catalyst for oxygen reduction reaction (ORR) which represents a key reaction at the cathodes of proton exchange membrane fuel cells, microbial fuel cells, and metal-air batteries.[1−8] Despite substantial progress, the identification of the active sites has remained a matter of active debates.[9−14] For instance, Wei et al. proposed that the catalytic active sites were carbon atoms adjacent to both pyridinic and pyrrolic N,[15] while Nakamura et al. claimed that the active sites were carbon atoms bonded to pyridinic N alone, after comparing the specific activity of N-doped highly oriented pyrolytic graphite.[1] Recently, Dai and co-workers suggested that graphitic N was actually responsible for ORR in three-dimensional (3D) interconnected N-doped graphene nanoribbon networks.[16] Determination of ORR active sites is not only critical in understanding the ORR mechanistic origin of N-doped carbons but also important in the rational design and optimization of N-doped carbon catalysts.[17−21] Such controversies are caused by several practical factors:

(i) A mixture of N-doping configurations is generally formed in the N-doped carbon catalysts.[22−27] To date, it remains a challenge to prepare N-doped carbons with a single nitrogen doping configuration, i.e., graphitic N, pyridinic N or pyrrolic N. Therefore, it is difficult to establish an unambiguous correlation between the ORR activity and a specific nitrogen doping configuration.

(ii) The ORR activity is dependent on multiple structural parameters, such as the morphology, work function of catalyst surface,[28] defect, degree of graphitization, and composition of the carbon catalysts; and the issue is

Received: January 25, 2018
Revised: June 3, 2018
Published: June 12, 2018

DOI: 10.1021/acscatal.8b00338
ACS Catal. 2018, 8, 6827−6836

further compounded by their inhomogeneity within the catalysts.[29−33]

(iii) Catalysts prepared even by the same research group can have batch-to-batch variations of their structure and activity. Therefore, it will be of fundamental significance to develop a reliable methodology where the ORR activity may be directly correlated with the structure of the catalysts.

This is the primary motivation of the present work.

Herein, by taking advantage of the observation that the ORR activity of N-doped carbons diminished during repeated potential cycling, we identified and quantified three nitrogen doping configurations by concurrently monitoring the carbon skeleton structures by XPS measurements, and observed a strong correlation between the ORR activity and the content of graphitic N in three carbon samples. In addition, density functional theory (DFT) calculations showed that the activation energy of the first electron reduction of O_2 adsorbed on carbon atoms adjacent to graphitic N was much lower than that on carbon atoms neighboring pyridinic or pyrrolic N. These results suggest that graphitic N is responsible for the ORR activity of N-doped carbons.

EXPERIMENTAL SECTION

Sample Preparation. Three N-doped carbons were prepared. The first one was prepared according to a method that we published earlier.[34] In a typical synthesis, 5.0 mL of pyrrole (99.98%) was dispersed in 30.0 mL of ethanol in a glass vial. In another vial, a solution was prepared by dissolving 1.0 g of poly(vinylpyrrolidone) (PVP-K30) in 30.0 mL of ethanol. These two solutions were then mixed under vigorous stirring, into which was added 20.0 g of NaCl crystals and dried at 70 °C. Then, 20.0 mL of a 0.85 M ammonium persulfate solution was added under mechanical stirring at 120 °C within 3.0 min. After being washed with deionized water to remove the NaCl crystals, the remaining solids were collected and thermally treated in a tube furnace at 800 °C for 4 h under a N_2 atmosphere, resulting in the formation of N-doped porous carbon nanosheets, which were referenced as N-PC.

The second sample, three-dimensional N-doped graphene nanoribbon networks, was prepared by following a literature procedure.[16] In a typical experiment, 2.0 g of melamine and 0.5 g of L-serine were mixed homogeneously in a ZrO_2 mortar. The resulting fine powders were then pyrolyzed at 600 °C for 2 h and at 1000 °C for another 2 h before being naturally cooled to room temperature in an Ar atmosphere at a gas flow rate of 300 sccm. The obtained sample was denoted as N-GRW.

The third sample, edge-rich N-doped graphene mesh, was prepared by adopting another procedure that was previously published.[35] Experimentally, 15.0 g of rice was washed by deionized water for several times and added into a glass flask with 500 mL of deionized water, and the mixture was boiled at 100 °C for 4.0 h. After removal of the precipitates via centrifugation, the obtained white emulsion was collected, into which 50.0 g of $MgCl_2{\cdot}6H_2O$, 7.5 g of melamine, and 100.0 mL of a NaOH (5.0 M) solution was added under vigorous stirring. The dispersion was heated at 60 °C until water was completely evaporated. The remaining white solids were collected and thermally treated in a tube furnace at 950 °C for 2 h under an Ar atmosphere, producing a black product that was ground into powders and washed with 6.0 M HCl solution at 80.0 °C to remove two-dimensional (2D) $Mg(OH)_2$ templates. The obtained sample was collected by filtering and drying in air and referenced as NGM.

Characterizations. Transmission electron microscopy (TEM) measurements were conducted on a Tecnai G2-F20 microscope at an acceleration voltage of 100 kV. TEM samples were prepared by dropcasting a catalyst dispersion directly onto a copper grid coated with a holey carbon film. X-ray photoelectron spectroscopy (XPS) measurements were performed on a PHI X-tool instrument. Raman spectra were recorded on a RENISHAW inVia instrument with an Ar laser source of 488 nm in a macroscopic configuration. Inductively coupled plasma−atomic emission spectrometry (ICP-AES) measurements were carried out with a Liberty-ax instrument.

Electrochemistry. All electrochemical measurements were performed on a CHI 750E electrochemical workstation in a conventional three-electrode cell, with a platinum wire serving as the counter electrode (note that the impact from Pt dissolution/deposition, if any, on the ORR performance is negligible; see Figure S1 in the Supporting Information), a Ag/AgCl electrode as the reference electrode, and a catalyst-modified glassy-carbon electrode (GCE) as the working electrode. The catalyst ink was prepared by adding 2.0 mg of the catalysts prepared above into a solution containing water, isopropanol, and Nafion (5%) at a volume ratio of 4:1:0.025 to form a homogeneous suspension at the catalyst concentration of 2.0 mg mL^{-1}. A calculated amount of the suspension was then evenly casted on the clean GCE surface with a syringe and dried in air, corresponding to a catalyst loading of 102.0 $\mu g\ cm^{-2}$ for N-PC, and 306.0 $\mu g\ cm^{-2}$ for both N-GRW and NGM. RRDE measurements were performed in the potential range of −0.03 V to +1.16 V vs RHE in an O_2-saturated 0.1 M KOH aqueous solution at various rates of rotation (100−2500 rpm). Cyclic voltammograms (CVs) were also acquired within this same potential range. Note that at least five identical GCE electrodes (same model RRDE from the same vendor) were prepared in the same manner from the same batch of catalyst ink. After voltammetric tests under the same conditions except for a different number of CV cycles, the catalysts were collected by using the following procedure:

(i) delamination of catalysts from the electrode surface by gentle scratching;

(ii) dispersion of the catalysts into deionized water; and

(iii) collection of the catalysts by centrifugation.

Steps (ii) and (iii) were repeated for several times to remove residual KOH. The purified catalysts were then transferred onto a conductive silicon wafer by using a pipet and dried in air, prior to XPS analysis. Electrochemical impedance spectra were recorded at the electrode potential of +0.85 V vs RHE, within the frequency range of 100 kHz to 0.01 Hz and an AC amplitude of 5 mV in 0.1 M KOH. Mott−Schottky analysis was carried out within the potential range of 0 to +1.2 V vs RHE at the AC frequency of 100 Hz and amplitude of 5 mV in 0.1 M KOH in the impedance-potential mode. Samples were collected after the potential cycling and characterized and analyzed.

In electrochemical measurements, the Ag/AgCl reference electrode was calibrated with respect to a reversible hydrogen electrode (RHE). The calibration was performed in a high-purity H_2 (99.999%) saturated electrolyte with two Pt wires as the working electrode and counter electrode, respectively. CVs were acquired at the scan rate of 50 mV s^{-1}, and the average of the two potentials at which the current crossed zero was taken as the thermodynamic potential for the RHE. In 0.1 M KOH, $E_{RHE} = E_{Ag/AgCl} + 0.965$ V.

Computational Methods. DFT calculations were performed with the open-source planewave code, Quantum Espresso.[36]

DOI: 10.1021/acscatal.8b00338
ACS Catal. 2018, 8, 6827−6836

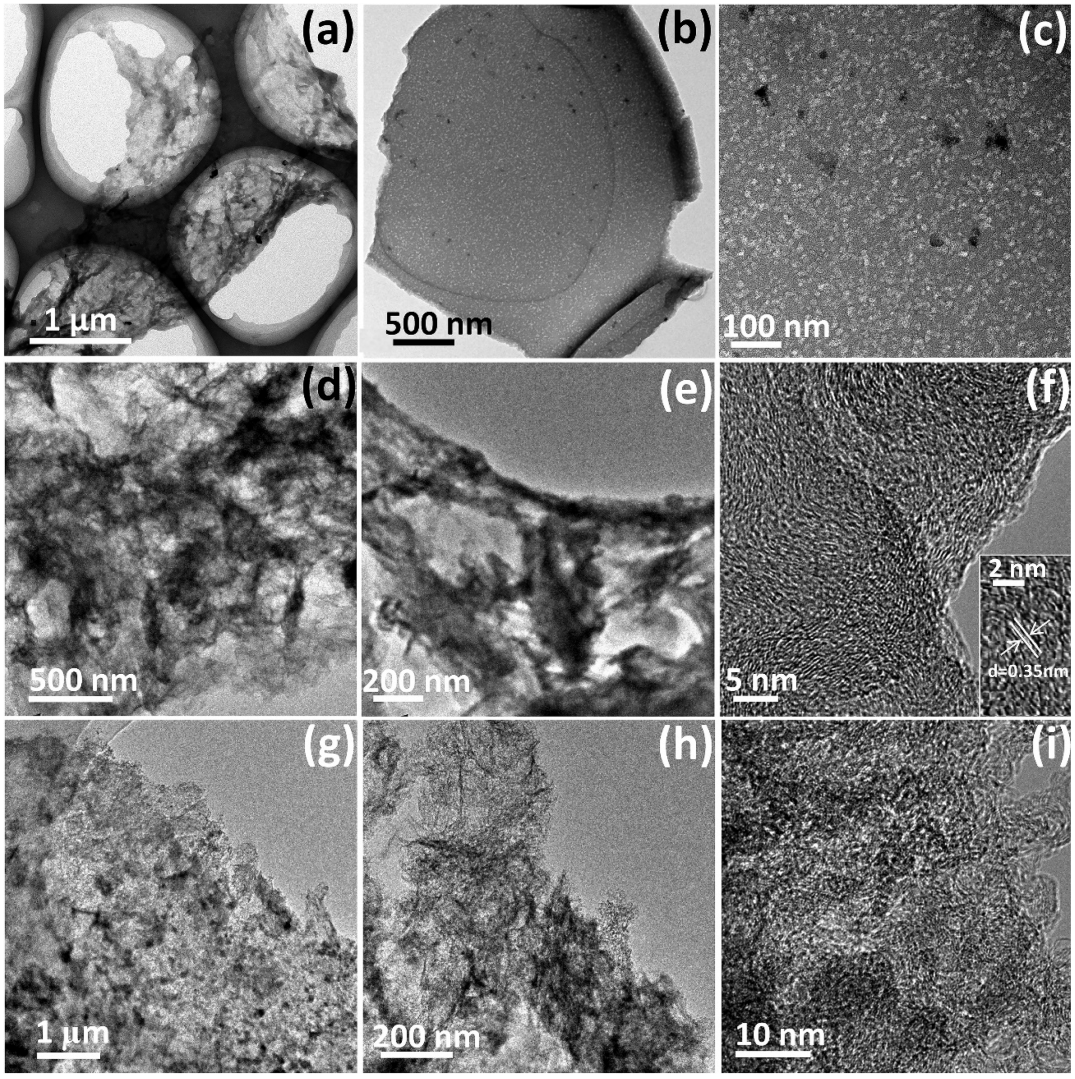

Figure 1. TEM images of (a, b, c) N-PC, (d, e, f) N-GRW, and (g, h, i) NGM samples at different magnifications. Inset to (f) is a zoom-in of the lattice fringes.

The vacuum thickness was set at ~14 Å to avoid interactions between periodic images. The ultrasoft pseudopotential[37] was adopted with the kinetic cutoff energy of 40 Ry (charge density cutoff 200 Ry), and 2 × 2 × 1 Monkhorst−Pack *K*-point grids[38] were sampled for the 2D supercell and 1 × 2 × 1 for the one-dimensional (1D) supercell to converge the total energy to the accuracy of 1 meV. The Marzari−Vanderbilt smearing was adopted with a smearing of 0.01 Ry. The electronic energy was converged to 10^{-8} Ry, and the force was converged to 10^{-4} a.u.

RESULTS AND DISCUSSION

Three N-doped carbon samples were prepared and studied. The first sample, N-PC, was prepared by controlled pyrolysis of polypyrrole nanosheets where ammonium persulfate was used as the polymerization initiator.[34,39,40] As shown in Figures 1a−c, N-PC displayed a sheetlike morphology comprising a large number of mesopores with a diameter of ~12.5 nm. The second sample, N-GRW,[16] as depicted in Figures 1d and 1e, displayed a crumpled nanoribbon network morphology. In the corresponding high-resolution TEM image (Figure 1f and inset), wavy strips with a fringe spacing of 0.350 nm can be observed, indicative of graphitization of the N-GRW sample. The third sample, NGM,[35] was prepared from rice with the aid of 2D $Mg(OH)_2$ templates. Figures 1g and 1h show that NGM consisted of a large number of ultrathin graphene flakes with a lateral size of ca. 200 nm. In the corresponding high-resolution TEM image, wavy strips with a *d*-spacing of 0.350 nm can be resolved, suggesting that NGM was largely graphitized. In addition, one can see that these graphene flakes were predominantly a few layers thick and contained abundant mesopores and in-plane cavities (Figure 1i). The results are consistent with those reported previously. ICP-AES measurements showed that the content of Fe was negligible in N-PC (0.61 ± 0.3 ppm) and NGM (4.0 ± 0.2 ppm), and was undetectable in N-GRW;[41,42] in addition, other metal elements, such as Co, Ni, Zn, Cr, Cd, and Mn, were also undetectable. These results suggest that the three catalysts can be considered as metal-free samples.

The ORR activity of N-PC was monitored by voltammetric measurements, where repeated potential cycling was carried out in an O_2-saturated 0.1 M KOH solution. From the RRDE voltammograms in Figure 2a, the limiting current can be found to diminish continuously; and concurrently, the onset potential showed a negative shift with increasing cycling number (see Figure S2 in the Supporting Information). Similar attenuation of the ORR activity can be observed with the N-GRW and NGM samples (see Figures S3 and S4 in the Supporting Informatiom).

DOI: 10.1021/acscatal.8b00338
ACS Catal. 2018, 8, 6827−6836

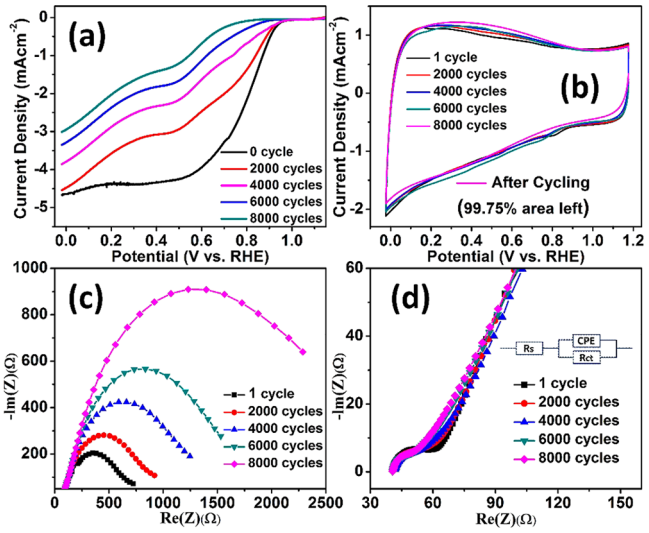

Figure 2. (a) RRDE voltammograms of N-PC at 1600 rpm after different CV cycles. (b) CVs acquired in a N_2-saturated 0.1 M KOH aqueous solution after different numbers of potential cycles in panel (a). Electrochemical impedance spectra of N-PC after different CV cycles in the low-frequency region (panel (c)) and the high-frequency region (panel (d)). Data were recorded at +0.85 V vs RHE, at the AC amplitude of 5 mV. The catalyst loading was 102 μg cm^{-2}, and the sweep rate was set at 50 mV s^{-1} in CV and 10 mV s^{-1} in RRDE measurements. The inset to panel (d) is an equivalent circuit where R_s is the (uncompensated) series resistance, R_{ct} the charge-transfer resistance, and CPE the constant-phase element, which is introduced to replace the double layer capacitance (C_d) to better describe the real capacitance of the electrode.

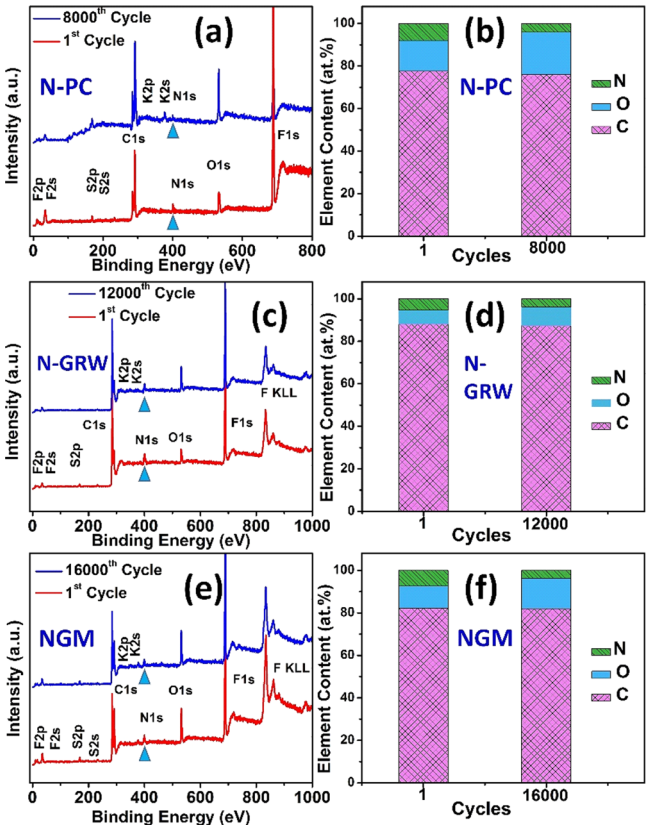

Figure 3. (a, c, e) XPS survey spectra and (b, d, f) the corresponding elemental relative contents of the various N-doped carbon samples after different cycles of RRDE scans.

The double-layer capacitive charging during ORR was also monitored by CV measurements. As shown in Figure 2b, the enclosed area of the CV curves was almost unchanged, with 99.75% retention even after 8000 CV cycles in the same O_2-saturated electrolyte for N-PC. The retention was similar for the other two carbon samples: 100.25% for N-GRW after 12 000 cycles (Figure S3) and 98.55% for NGM after 16 000 cycles (Figure S4). These observations indicate that, although the surface area of the carbon catalysts remained virtually unchanged, the ORR activities diminished markedly with repeated potential cycling.[34]

In the corresponding electrochemical impedance measurements, the diameter of the semicircle observed in the low-frequency region increased drastically as the number of cycles increased (see Figure 2c, as well as Figures S3d and S4d), indicative of an increase of the charge-transfer resistance (R_{ct}) in the three samples, whereas the x-axis intercept (R_s) of the semicircle was virtually identical, suggesting no apparent change of the electrical conductivity of the catalysts during repeated potential cycling. Furthermore, in the high-frequency region (see Figure 2d, as well as Figures S3e and S4e), the slopes for all the impedance curves are highly comparable, consistent with the almost invariant double-layer capacitance (i.e., electrochemical surface area), as observed above. Therefore, the attenuation of the ORR activity was most likely due to the loss of active sites but not the surface area or electrical conductivity of the catalysts.

The corresponding structural evolution of the carbon samples was then examined by XPS measurements. For the XPS survey spectra (see Figures 3a, 3c, and 3e), C, N, and O elements can be readily identified in the as-prepared carbon samples (the K, F, and S elements arose from residual KOH and Nafion). Yet, two obvious differences can be seen after prolonged cycling (Figure 3b, 3d, and 3f). First, the N 1s peak intensity diminished significantly and became almost undetectable after, for instance, 8000 cycles for N-PC, 12 000 cycles for N-GRW, and 16 000 cycles for NGM. Second, the intensity of the O 1s peak increased only slightly, suggesting that, although the oxidation of carbon is inevitable during prolonged potential cycling, the corrosion kinetic is slow in alkaline electrolytes.[43] In fact, from Figure 3b, 3d, and 3f, one can see that the content of elemental carbon in the three samples is almost unchanged, and the oxygen content increased only by 5.5 at. % for N-PC after 8000 cycles, 2.3 at. % for N-GRW after 12 000 cycles, and 4.0 at. % for NGM after 16 000 cycles. The results indicate that, indeed, only a small fraction of the carbon materials was electrochemically corroded during prolonged potential cycling.

Figure 4a depicts the high-resolution scans of the N 1s electrons in the N-PC catalyst. It can be seen that the intensity decreased substantially after 8000 cycles, suggesting an apparent loss of nitrogen from the carbon skeletons during prolonged cycling. Deconvolution of the N 1s spectra yields four peaks at 398.2, 399.4, 400.8, and 402.7 eV, corresponding to the pyridinic, pyrrolic, graphitic, and oxidized N (Figure 4b), respectively.[16,18,44,45] Notably, the concentrations of these four types of nitrogen dopants showed a different evolution trend with potential cycling. As depicted in Figure 4c, oxidized N and pyrrolic N represented only 0.20 at. % and 0.76 at. % in the as-prepared N-PC catalyst, respectively, and decreased slightly to 0.17 at. % and 0.61 at. % after 8000 cycles, suggesting their high electrochemical stability in alkaline electrolytes.[39,40] For graphitic N, the content was 4.47 at. % before ORR tests, the highest among the four nitrogen dopants; yet, during ORR cycling, it decreased gradually, showing a diminishing rate that

DOI: 10.1021/acscatal.8b00338
ACS Catal. 2018, 8, 6827−6836

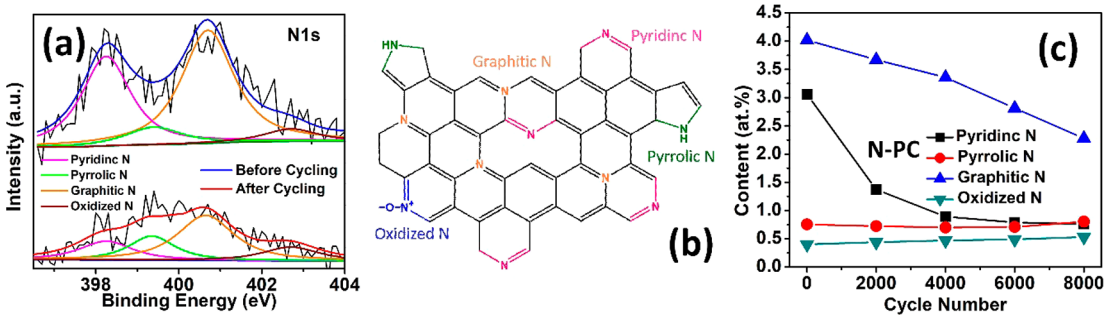

Figure 4. (a) High-resolution XPS scans of the N 1s electrons in N-PC before and after 8000 cycling tests; (b) illustration of the four nitrogen doping configurations; and (c) the content of N dopants in N-PC after various potential cycles.

was greater than that of pyrrolic N. The changing trend for pyridinic N was somewhat more complex. About half of the pyridinic N was lost in the first 2000 cycles (to 1.20 at. % from the initial 2.75 at. %), suggesting relatively low electrochemical stability.[14,46] The next 2000 cycles saw an additional loss of $\sim^1/_5$ of the original pyridinic N content. Yet, after 4000 more cycles, the loss of pyridinic N became small, with a final concentration of 0.45 at. %.

Since XPS is a surface-sensitive tool, to further check if the bulk shows similar diminishment dynamics of the three types of nitrogen dopants, Mott−Schottky experiments[16] were conducted. According to the Mott−Schottky theory, for *n*- and *p*-type dopants in graphitic carbons, the correlation between space-charge limiting capacitance (C_{SCL}) and the density of dopants in materials can be depicted by eqs 1 and 2, respectively,

n-type doping:

$$C_{SCL}^{-2} = \frac{2}{eA^2N_d\varepsilon\varepsilon_0}\left(E - E_{fb} - \frac{kT}{e}\right) \quad (1)$$

p-type doping:

$$C_{SCL}^{-2} = \frac{-2}{eA^2N_d\varepsilon\varepsilon_0}\left(E - E_{fb} + \frac{kT}{e}\right) \quad (2)$$

where ε is the dielectric constant of the material, ε_0 the permittivity of free space, A the area, e the elementary charge, N_d the density of dopants, E the applied potential, E_{fb} the flat-band potential, k the Boltzmann constant, and T the absolute temperature. Experimentally, C_{SCL} can be determined by eq 3,[47,48]

$$C_{SCL} = -\frac{1}{\omega Z_{img}} \quad (3)$$

where Z_{img} is the imaginary component of the impedance and ω is the angular frequency ($\omega = 2\pi f$). From Figures 5a and 5b, one can indeed see linear variations of C_{SCL}^{-2} versus electrode potential with a positive and negative slope in the low and high potential region, respectively, indicative of the formation of *n*- and *p*-type nitrogen dopants in the N-PC sample. Generally, graphitic and pyrrolic nitrogens are *n*-type dopants and pyridinic nitrogens are *p*-type dopants.[14,49,50] Note that the trace amount of oxidized nitrogens are believed to be inactive for ORR and, hence, are not considered in the Mott−Schottky measurements. Because e, ε, and ε_0 are constants, and the surface area A of the catalyst is almost unchanged during potential cycling, as manifested in CV measurements (see Figure 2b, as well as Figures S3c and S4c), from eqs 1 and 2, one can see that the slope of the linear regression is inversely proportional to N_d.

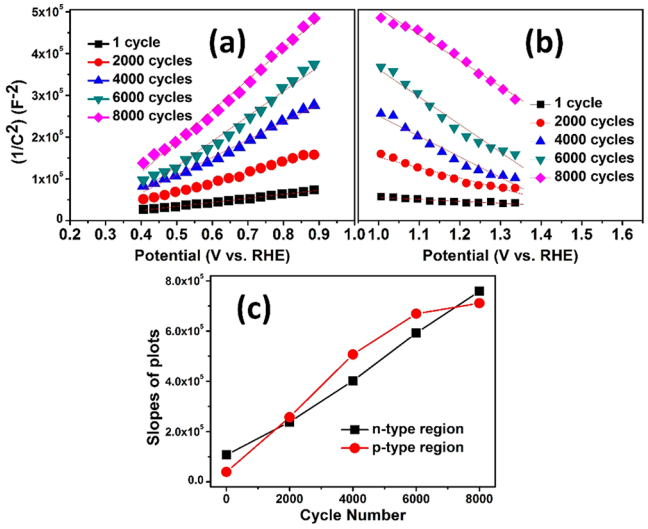

Figure 5. Mott−Schottky analysis of N-PC conducted at the frequency of 100 Hz in Ar-saturated 0.1 M KOH with a catalyst loading of 102 μg cm^{-2} on a glassy carbon electrode. The plots of C_{SCL}^{-2} versus potential E show (a) positive and (b) negative slopes for the N-PC sample after different numbers of potential cycles. (c) Plots of absolute slopes observed in panels (a) and (b) against cycling number.

From Figure 5a, the slopes of the Mott−Schottky plots for the N-PC sample after 1, 2000, 4000, 6000 and 8000 cycles in the *n*-type region are estimated to be 1.07×10^5, 2.38×10^5, 4.02×10^5, 5.92×10^5, and 7.58×10^5 F^{-2} V, respectively; while the slopes in the *p*-type region (Figure 5b) are -0.48×10^5, -2.57×10^5, -5.17×10^5, -6.69×10^5, and -7.11×10^5 F^{-2} V, respectively. When the absolute values of these slopes were plotted against potential cycle number (Figure 5c), an almost-linear variation was observed in the *n*-type region, which indicates that *n*-type N (i.e., graphitic and pyrrolic N) diminished at the same rate during the cycling tests. By sharp contrast, the plot in the *p*-type region showed two distinct segments. In the first 4000 cycles, a linear plot was observed with a higher slope than that observed in the *n*-type region. However, in the next 4000 cycles, the plot deviated from the linear curve and gradually reached a plateau. These results signified that the diminishment rate of *p*-type N (i.e., pyridinic N) was higher than that of *n*-type N (graphitic and pyrrolic N) in the first 4000 cycles, while it became lower than that of *n*-type N in the subsequent 4000 cycles, consistent with the XPS results in Figure 4c. These observations signify that the diminishing trends of the three types of nitrogen doping configurations determined by XPS are consistent with those identified by Mott−Schottky analysis.

DOI: 10.1021/acscatal.8b00338
ACS Catal. 2018, 8, 6827−6836

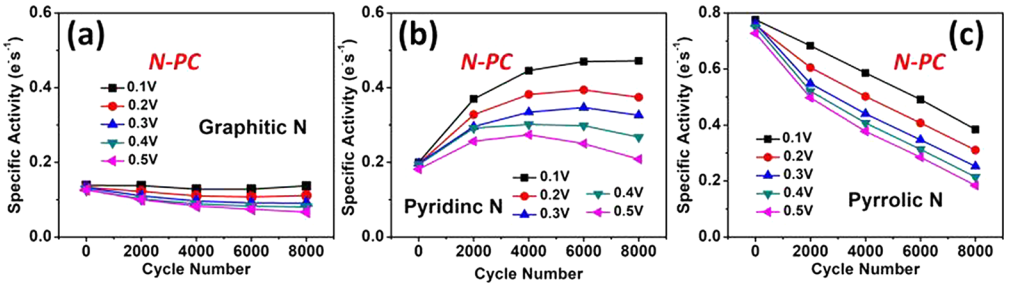

Figure 6. Plots of the specific activity of (a) graphitic N, (b) pyridinic N, and (c) pyrrolic N in N-PC versus potential cycle number.

Furthermore, from the plots of the number of electron transfer (n) vs cycle number in Figure S5a in the Supporting Information, one can find that, during the entire cycling measurements, the n values remained close to 4 in a wide range of potentials, which suggests that, in alkaline aqueous solution, the ORR process on N-PC largely followed the 4e$^-$ reaction pathway (see eq 4):

$$O_2 + 2H_2O + 4e^- \rightarrow 4OH^- \quad (4)$$

That is, the effectiveness of oxygen reduction was not compromised during prolonged cycling, and the diminishing ORR performance was most likely due to a gradual loss of catalytic active centers, since the electrolyte solution remained saturated with oxygen. Therefore, one can predict that, if a specific nitrogen, for example, graphitic N, is responsible for the ORR activity of the N-doped carbons, the diminishment of the ORR current should correlate with the loss of the corresponding N-dopant. This can be manifested by comparing the specific activity (a) of the various N dopants (i.e., pyridinic, pyrrolic, or graphitic N), which is defined as

$$a = \frac{\text{ORR current density}}{\text{specific N dopant density}} \quad (5)$$

As summarized in Figure 6a, the specific activity of graphitic N was largely invariant over 8000 potential cycles, which was estimated to be 0.137 e$^-$ s^{-1} $N_{\text{graphitic}}{}^{-1}$ for the first cycle, 0.138 e$^-$ s^{-1} $N_{\text{graphitic}}{}^{-1}$ after 2000 cycles, 0.128 e$^-$ s^{-1} $N_{\text{graphitic}}{}^{-1}$ after 4000 cycles, 0.128 e$^-$ s^{-1} $N_{\text{graphitic}}{}^{-1}$ after 6000 cycles and 0.131 e$^-$ s^{-1} $N_{\text{graphitic}}{}^{-1}$ after 8000 cycles at +0.10 V, all very close to results reported in the literature.[1,16,39,51,52] The slight decrease of the specific activity for graphitic N during prolonged cycling is likely due to the gradual corrosion of carbon in the catalyst. By sharp contrast, the specific activity per pyridinic N (Figure 6b) and pyrrolic N (Figure 6c) in the N-PC catalyst varied significantly during the cycling tests. This observation signifies that ORR activity was largely determined by graphitic N.

Polarization curves for N-PC on a nonrotating glassy carbon electrode also showed similar results (see Figure S6 in the Supporting Information), where, among the three N dopants, only graphitic N showed an almost-constant specific activity during prolonged potential cycling.

Taken together, the above results strongly suggest that graphitic N is responsible for the ORR activity of N-doped carbons. This conclusion coincides with our previous observations[39,53] that N-doped carbons with the highest content of graphitic N showed the highest ORR activity, and is also consistent with results reported recently by Dai et al.[16] In fact, similar changing trends of the specific activity were also observed in two other metal-free samples, N-GRW and NGM, which were synthesized by adopting literature protocols.[16,35] Although the exact ORR performance (see Figures S3–S5 in the Supporting Information) and diminishing trend of nitrogen dopants (see Figures S7 and S8 in the Supporting Information) for N-GRW and NGM are different from those of N-PC during potential cycling, only graphitic N in both N-GRW and NGM samples maintained an almost-unchanged specific activity, while pyridinic and pyrrolic N showed a distinct variation of the specific activity (see Figure 7). These results further confirm that graphitic N is mostly likely responsible for the ORR activity on N-doped carbons. Importantly, the consistent observations suggest that the attenuation method described above may be exploited as a generic procedure to identify ORR active centers of N-doped carbons.

To further confirm the active sites of N-doped carbons, we carried out DFT calculations to investigate the activity of various atoms in N-doped carbon. Generally, the 4-electron ORR mechanism on carbon materials is believed to proceed via the following steps:[54−56]

$$O_2 + * + H_2O(l) + e^- \rightarrow OOH^* + OH^- \quad (6)$$

$$OOH^* + e^- \rightarrow O^* + OH^- \quad (7)$$

$$O^* + H_2O(l) + e^- \rightarrow OH^* + OH^- \quad (8)$$

$$OH^* + e^- \rightarrow OH^- + * \quad (9)$$

where asterisks indicate active sites. The various oxygen intermediates such as OOH*, O*, and OH* adsorbed on N-doped carbons is shown in Figure 8a. Previous studies have shown that step (6) is most likely the rate-determining step, as manifested in Tafel analysis (see Figure S9 in the Supporting Information).[57,58] For sp^2 carbon (even with nitrogen doping), the lack of electron spin and relatively small density of states around the Fermi level makes it difficult for oxygen species to adsorb onto the active site and reduce to OOH.[59,60] Therefore, the reaction Gibbs free energy of this step (ΔG_1) was quantitatively estimated to compare the performance of the different types of nitrogen doping configurations. As has been shown, only the nearest-neighbor carbons of nitrogen dopants might serve as the active sites,[58,59,61] and thus the calculations were focused on carbon atoms adjacent to the nitrogen dopants. As shown in Figure 8b, the neighboring carbons (denoted by dashed squares) of graphitic nitrogen show a ΔG_1 value of 1.34 eV, which is much lower than those of pyrrolic N (1.56 eV) and pyridinic N (1.50 and 1.88 eV). This suggests that the carbon atoms adjacent to graphitic N are most likely responsible for the ORR activity, in good agreement with the above experiment results.

To examine the structural change during the ORR process, we optimized the catalyst structure after the adsorption of oxygen intermediates onto these carbon atoms and carefully examined the C−N bond length. From Figure S10 in the Supporting Information, it can be seen that, for graphitic N, the C−N bond

DOI: 10.1021/acscatal.8b00338
ACS Catal. 2018, 8, 6827−6836

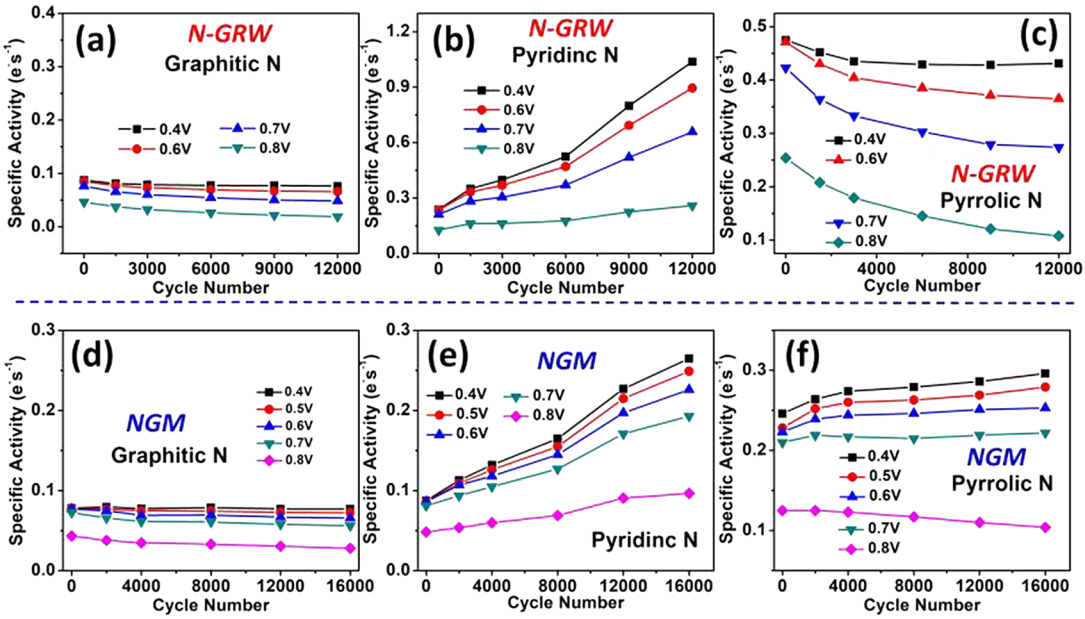

Figure 7. Plots of the specific activity against cycling number for (a, d) graphitic N, (b, e) pyridinic N, and (c, f) pyrrolic N in N-GRW (panels (a–c)) and NGM (panels (d–f)).

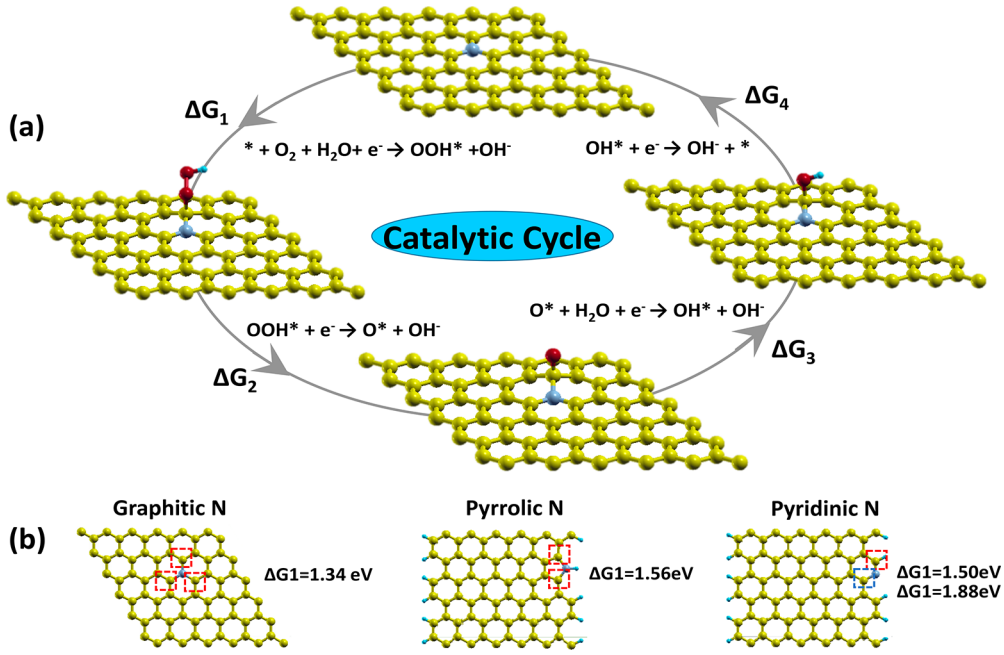

Figure 8. (a) Schematic illustration of the $4e^-$ pathways of ORR on N-doped carbon. (b) Schematic illustration of the three nitrogen doping configurations and the corresponding ΔG_1 values in the first-electron reduction process.

length is 1.4109 Å for the clean catalysts; yet, when oxygen species (OOH, O, and OH) were adsorbed onto the adjacent carbon sites, it increased to 1.4700, 1.6034, and 1.4981 Å, respectively, and the other two C–N bonds without oxygen adsorption showed a decrease of the bond length to 1.4044, 1.3804, and 1.4011 Å, respectively. Note that the bond length of 1.6034 Å (Figure S10b) is even 0.13 Å longer than that of traditional C–N single bond.[62] This suggests that one of the C–N bonds might break during ORR (Figure S11 in the Supporting Information), and the resultant structures react further with electrolyte species, leading to irreversible degradation of the catalysts and, hence, the attenuation of the ORR activity.

CONCLUSION

In summary, prolonged potential cycling was performed to examine the ORR activity of metal-free N-doped carbons, where the ORR activity was found to attenuate with potential cycles and the attenuation was correlated with the diminishing concentration of graphitic N in the catalysts. The specific activity per graphitic N was found to remain unchanged during prolonged potential cycling within a wide range of potentials, and comparable to the value in the first cycle, in good agreement with theoretical prediction. This is in marked contrast to results of pyridinic and pyrrolic N, where an apparent variation of the corresponding specific activity was observed with potential cycling.

DOI: 10.1021/acscatal.8b00338
ACS Catal. 2018, 8, 6827–6836

DFT calculations showed a lower Gibbs free-energy change for the first-electron reduction of oxygen, a rate-determining step in the $4e^-$ ORR process, on carbon atoms adjacent to graphitic N, compared to that for pyridinic and pyrrolic N. Taken together, these results strongly suggest that graphitic N is responsible for the ORR activity of N-doped carbons. This procedure based on the attenuation of catalytic activity may be exploited as a generic, effective method in the determination of catalytic active sites in heteroatom-doped carbons and, more significantly, provides a fundamental framework in the design and engineering of efficient, long-lasting carbon-based catalysts for important electrochemical reactions in energy conversion and storage.

Note that the ORR active site for N-doped carbons in acidic electrolytes is not necessarily identical to that in alkaline electrolytes. Determination of ORR active sites for N-doped carbons in acidic electrolytes is ongoing, and results will be published in due course.

■ ASSOCIATED CONTENT

Supporting Information

The Supporting Information is available free of charge on the ACS Publications website at DOI: 10.1021/acscatal.8b00338.

Additional experimental data including LSV curves, XPS results, Tafel plots, plots of number of electron transfer and peroxide yield, Mott−Schottky analysis, and DFT calculations (PDF)

■ AUTHOR INFORMATION

Corresponding Authors

*E-mail: esguili@scut.edu (L. Li).
*E-mail: shaowei@ucsc.edu (S. Chen).

ORCID

Ligui Li: 0000-0002-1636-9342
Zhenghua Tang: 0000-0003-0718-3164
Xiongwu Kang: 0000-0003-2587-4962
Shaowei Chen: 0000-0002-3668-8551

Author Contributions

The manuscript was written through contributions of all authors. All authors have given approval to the final version of the manuscript.

Notes

The authors declare no competing financial interest.

■ ACKNOWLEDGMENTS

This work was supported by the National Natural Science Foundation of China (Nos. 21528301 and 51402111), Guangdong Innovative and Entrepreneurial Research Team Program (No. 2014ZT05N200), and the Fundamental Research Funds for the Central Universities (No. 2015zz/05). S.W.C. thanks National Science Foundation for partial support of the work (Nos. CHE-1710408 and DMR-1409396). This work used the Extreme Science and Engineering Discovery Environment (XSEDE), which is supported by the National Science Foundation (No. ACI-1548562).

■ REFERENCES

(1) Guo, D. H.; Shibuya, R.; Akiba, C.; Saji, S.; Kondo, T.; Nakamura, J. Active sites of nitrogen-doped carbon materials for oxygen reduction reaction clarified using model catalysts. *Science* **2016**, *351*, 361−365.

(2) Ganesan, P.; Prabu, M.; Sanetuntikul, J.; Shanmugam, S. Cobalt sulfide nanoparticles grown on nitrogen and sulfur codoped graphene oxide: an efficient electrocatalyst for oxygen reduction and evolution reactions. *ACS Catal.* **2015**, *5*, 3625−3637.

(3) Chen, S.; Duan, J.; Jaroniec, M.; Qiao, S. Z. Three-Dimensional N-Doped Graphene Hydrogel/NiCo Double Hydroxide Electrocatalysts for Highly Efficient Oxygen Evolution. *Angew. Chem., Int. Ed.* **2013**, *52*, 13567−13570.

(4) Li, Q.; Cao, R.; Cho, J.; Wu, G. Nanocarbon electrocatalysts for oxygen reduction in alkaline media for advanced energy conversion and storage. *Adv. Energy Mater.* **2014**, *4*, 1301415.

(5) Wu, G.; Mack, N. H.; Gao, W.; Ma, S.; Zhong, R.; Han, J.; Baldwin, J. K.; Zelenay, P. Nitrogen-doped graphene-rich catalysts derived from heteroatom polymers for oxygen reduction in nonaqueous lithium−O_2 battery cathodes. *ACS Nano* **2012**, *6*, 9764−9776.

(6) Ma, T. Y.; Ran, J.; Dai, S.; Jaroniec, M.; Qiao, S. Z. Phosphorus-Doped Graphitic Carbon Nitrides Grown In Situ on Carbon-Fiber Paper: Flexible and Reversible Oxygen Electrodes. *Angew. Chem., Int. Ed.* **2015**, *54*, 4646−4650.

(7) Hong, W. T.; Risch, M.; Stoerzinger, K. A.; Grimaud, A.; Suntivich, J.; Shao-Horn, Y. Toward the rational design of non-precious transition metal oxides for oxygen electrocatalysis. *Energy Environ. Sci.* **2015**, *8*, 1404−1427.

(8) Liang, Y.; Li, Y.; Wang, H.; Zhou, J.; Wang, J.; Regier, T.; Dai, H. Co_3O_4 nanocrystals on graphene as a synergistic catalyst for oxygen reduction reaction. *Nat. Mater.* **2011**, *10*, 780−786.

(9) Subramanian, N. P.; Li, X.; Nallathambi, V.; Kumaraguru, S. P.; Colon-Mercado, H.; Wu, G.; Lee, J.-W.; Popov, B. N. Nitrogen-modified carbon-based catalysts for oxygen reduction reaction in polymer electrolyte membrane fuel cells. *J. Power Sources* **2009**, *188*, 38−44.

(10) Rao, C. V.; Cabrera, C. R.; Ishikawa, Y. In search of the active site in nitrogen-doped carbon nanotube electrodes for the oxygen reduction reaction. *J. Phys. Chem. Lett.* **2010**, *1*, 2622−2627.

(11) Qu, L.; Liu, Y.; Baek, J.-B.; Dai, L. Nitrogen-doped graphene as efficient metal-free electrocatalyst for oxygen reduction in fuel cells. *ACS Nano* **2010**, *4*, 1321−1326.

(12) Xing, T.; Zheng, Y.; Li, L. H.; Cowie, B. C.; Gunzelmann, D.; Qiao, S. Z.; Huang, S.; Chen, Y. Observation of active sites for oxygen reduction reaction on nitrogen-doped multilayer graphene. *ACS Nano* **2014**, *8*, 6856−6862.

(13) Liang, H.-W.; Zhuang, X.; Brüller, S.; Feng, X.; Müllen, K. Hierarchically porous carbons with optimized nitrogen doping as highly active electrocatalysts for oxygen reduction. *Nat. Commun.* **2014**, *5*, 4973.

(14) Lai, L.; Potts, J. R.; Zhan, D.; Wang, L.; Poh, C. K.; Tang, C.; Gong, H.; Shen, Z.; Lin, J.; Ruoff, R. S. Exploration of the active center structure of nitrogen-doped graphene-based catalysts for oxygen reduction reaction. *Energy Environ. Sci.* **2012**, *5*, 7936−7942.

(15) Ding, W.; Wei, Z.; Chen, S.; Qi, X.; Yang, T.; Hu, J.; Wang, D.; Wan, L. J.; Alvi, S. F.; Li, L. Space-Confinement-Induced Synthesis of Pyridinic- and Pyrrolic-Nitrogen-Doped Graphene for the Catalysis of Oxygen Reduction. *Angew. Chem., Int. Ed.* **2013**, *52*, 11755−11759.

(16) Yang, H. B.; Miao, J.; Hung, S.-F.; Chen, J.; Tao, H. B.; Wang, X.; Zhang, L.; Chen, R.; Gao, J.; Chen, H. M.; Dai, L.; Liu, B. Identification of catalytic sites for oxygen reduction and oxygen evolution in N-doped graphene materials: Development of highly efficient metal-free bifunctional electrocatalyst. *Sci. Adv.* **2016**, *2*, e1501122.

(17) He, W.; Jiang, C.; Wang, J.; Lu, L. High-Rate Oxygen Electroreduction over Graphitic-N Species Exposed on 3D Hierarchically Porous Nitrogen-Doped Carbons. *Angew. Chem., Int. Ed.* **2014**, *53*, 9503−9507.

(18) Geng, D.; Chen, Y.; Chen, Y.; Li, Y.; Li, R.; Sun, X.; Ye, S.; Knights, S. High oxygen-reduction activity and durability of nitrogen-doped graphene. *Energy Environ. Sci.* **2011**, *4*, 760−764.

(19) Hu, C.; Dai, L. Multifunctional Carbon-Based Metal-Free Electrocatalysts for Simultaneous Oxygen Reduction, Oxygen Evolution, and Hydrogen Evolution. *Adv. Mater.* **2017**, *29*, 1604942.

(20) Huang, S.; Meng, Y.; He, S.; Goswami, A.; Wu, Q.; Li, J.; Tong, S.; Asefa, T.; Wu, M. N-, O-, and S-Tridoped Carbon-Encapsulated

DOI: 10.1021/acscatal.8b00338
ACS Catal. 2018, 8, 6827−6836

Co_9S_8 Nanomaterials: Efficient Bifunctional Electrocatalysts for Overall Water Splitting. *Adv. Funct. Mater.* **2017**, *27*, 1606585.
(21) Liu, Q.; Wang, Y.; Dai, L.; Yao, J. Scalable Fabrication of Nanoporous Carbon Fiber Films as Bifunctional Catalytic Electrodes for Flexible Zn-Air Batteries. *Adv. Mater.* **2016**, *28*, 3000−3006.
(22) Lee, W. J.; Maiti, U. N.; Lee, J. M.; Lim, J.; Han, T. H.; Kim, S. O. Nitrogen-doped carbon nanotubes and graphene composite structures for energy and catalytic applications. *Chem. Commun.* **2014**, *50*, 6818−6830.
(23) Ai, K.; Liu, Y.; Ruan, C.; Lu, L.; Lu, G. M. Sp2 C-Dominant N-Doped Carbon Sub-micrometer Spheres with a Tunable Size: A Versatile Platform for Highly Efficient Oxygen-Reduction Catalysts. *Adv. Mater.* **2013**, *25*, 998−1003.
(24) Gong, K.; Du, F.; Xia, Z.; Durstock, M.; Dai, L. Nitrogen-doped carbon nanotube arrays with high electrocatalytic activity for oxygen reduction. *Science* **2009**, *323*, 760−764.
(25) Tan, Y. M.; Xu, C. F.; Chen, G. X.; Fang, X. L.; Zheng, N. F.; Xie, Q. J. Facile Synthesis of Manganese-Oxide-Containing Mesoporous Nitrogen-Doped Carbon for Efficient Oxygen Reduction. *Adv. Funct. Mater.* **2012**, *22*, 4584−4591.
(26) Wang, S. Y.; Iyyamperumal, E.; Roy, A.; Xue, Y. H.; Yu, D. S.; Dai, L. M. Vertically Aligned BCN Nanotubes as Efficient Metal-Free Electrocatalysts for the Oxygen Reduction Reaction: A Synergetic Effect by Co-Doping with Boron and Nitrogen. *Angew. Chem., Int. Ed.* **2011**, *50*, 11756−11760.
(27) Men, B.; Sun, Y.; Li, M.; Hu, C.; Zhang, M.; Wang, L.; Tang, Y.; Chen, Y.; Wan, P.; Pan, J. Hierarchical Metal-Free Nitrogen-Doped Porous Graphene/Carbon Composites as an Efficient Oxygen Reduction Reaction Catalyst. *ACS Appl. Mater. Interfaces* **2016**, *8*, 1415−1423.
(28) Cheon, J. Y.; Kim, J. H.; Kim, J. H.; Goddeti, K. C.; Park, J. Y.; Joo, S. H. Intrinsic relationship between enhanced oxygen reduction reaction activity and nanoscale work function of doped carbons. *J. Am. Chem. Soc.* **2014**, *136*, 8875−8878.
(29) Nam, G.; Park, J.; Kim, S. T.; Shin, D.-b.; Park, N.; Kim, Y.; Lee, J.-S.; Cho, J. Metal-free Ketjenblack incorporated nitrogen-doped carbon sheets derived from gelatin as oxygen reduction catalysts. *Nano Lett.* **2014**, *14*, 1870−1876.
(30) Wei, W.; Liang, H.; Parvez, K.; Zhuang, X.; Feng, X.; Müllen, K. Nitrogen-Doped Carbon Nanosheets with Size-Defined Mesopores as Highly Efficient Metal-Free Catalyst for the Oxygen Reduction Reaction. *Angew. Chem.* **2014**, *126*, 1596−1600.
(31) Chen, S.; Bi, J.; Zhao, Y.; Yang, L.; Zhang, C.; Ma, Y.; Wu, Q.; Wang, X.; Hu, Z. Nitrogen-Doped Carbon Nanocages as Efficient Metal-Free Electrocatalysts for Oxygen Reduction Reaction. *Adv. Mater.* **2012**, *24*, 5593−5597.
(32) Yan, X.; Jia, Y.; Chen, J.; Zhu, Z.; Yao, X. Defective-Activated-Carbon-Supported Mn−Co Nanoparticles as a Highly Efficient Electrocatalyst for Oxygen Reduction. *Adv. Mater.* **2016**, *28*, 8771−8778.
(33) Jia, Y.; Zhang, L.; Du, A.; Gao, G.; Chen, J.; Yan, X.; Brown, C. L.; Yao, X. Defect graphene as a trifunctional catalyst for electrochemical reactions. *Adv. Mater.* **2016**, *28*, 9532−9538.
(34) Niu, W.; Li, L.; Wang, N.; Zeng, S.; Liu, J.; Zhao, D.; Chen, S. Volatilizable template-assisted scalable preparation of honeycomb-like porous carbons for efficient oxygen electroreduction. *J. Mater. Chem. A* **2016**, *4*, 10820−10827.
(35) Tang, C.; Wang, H. F.; Chen, X.; Li, B. Q.; Hou, T. Z.; Zhang, B.; Zhang, Q.; Titirici, M. M.; Wei, F. Topological Defects in Metal-Free Nanocarbon for Oxygen Electrocatalysis. *Adv. Mater.* **2016**, *28*, 6845−6851.
(36) Giannozzi, P.; Baroni, S.; Bonini, N.; Calandra, M.; Car, R.; Cavazzoni, C.; Ceresoli, D.; Chiarotti, G. L.; Cococcioni, M.; Dabo, I.; Dal Corso, A.; de Gironcoli, S.; Fabris, S.; Fratesi, G.; Gebauer, R.; Gerstmann, U.; Gougoussis, C.; Kokalj, A.; Lazzeri, M.; Martin-Samos, L.; Marzari, N.; Mauri, F.; Mazzarello, R.; Paolini, S.; Pasquarello, A.; Paulatto, L.; Sbraccia, C.; Scandolo, S.; Sclauzero, G.; Seitsonen, A. P.; Smogunov, A.; Umari, P.; Wentzcovitch, R. M. QUANTUM ESPRESSO: A modular and open-source software project for quantum simulations of materials. *J. Phys.: Condens. Matter* **2009**, *21*, 395502.
(37) Garrity, K. F.; Bennett, J. W.; Rabe, K. M.; Vanderbilt, D. Pseudopotentials for high-throughput DFT calculations. *Comput. Mater. Sci.* **2014**, *81*, 446−452.
(38) Marzari, N.; Vanderbilt, D.; De Vita, A.; Payne, M. C. Thermal contraction and disordering of the Al(110) surface. *Phys. Rev. Lett.* **1999**, *82*, 3296−3299.
(39) Niu, W.; Li, L.; Liu, X.; Wang, N.; Liu, J.; Zhou, W.; Tang, Z.; Chen, S. Mesoporous N-doped carbons prepared with thermally removable nanoparticle templates: an efficient electrocatalyst for oxygen reduction reaction. *J. Am. Chem. Soc.* **2015**, *137*, 5555−5562.
(40) Niu, W.; Li, L.; Liu, J.; Wang, N.; Li, W.; Tang, Z.; Zhou, W.; Chen, S. Graphene-Supported Mesoporous Carbons Prepared with Thermally Removable Templates as Efficient Catalysts for Oxygen Electroreduction. *Small* **2016**, *12*, 1900−1908.
(41) Masa, J.; Zhao, A.; Xia, W.; Sun, Z.; Mei, B.; Muhler, M.; Schuhmann, W. Trace metal residues promote the activity of supposedly metal-free nitrogen-modified carbon catalysts for the oxygen reduction reaction. *Electrochem. Commun.* **2013**, *34*, 113−116.
(42) Ye, R.; Dong, J.; Wang, L.; Mendoza-Cruz, R.; Li, Y.; An, P.-F.; Yacamán, M. J.; Yakobson, B. I.; Chen, D.; Tour, J. M. Manganese deception on graphene and implications in catalysis. *Carbon* **2018**, *132*, 623−631.
(43) Varcoe, J. R.; Atanassov, P.; Dekel, D. R.; Herring, A. M.; Hickner, M. A.; Kohl, P. A.; Kucernak, A. R.; Mustain, W. E.; Nijmeijer, K.; Scott, K.; Xu, T.; Zhuang, L. Anion-exchange membranes in electrochemical energy systems. *Energy Environ. Sci.* **2014**, *7*, 3135−3191.
(44) Li, Q.; Zhang, S.; Dai, L.; Li, L.-s. Nitrogen-doped colloidal graphene quantum dots and their size-dependent electrocatalytic activity for the oxygen reduction reaction. *J. Am. Chem. Soc.* **2012**, *134*, 18932−18935.
(45) Chen, P.; Wang, L.-K.; Wang, G.; Gao, M.-R.; Ge, J.; Yuan, W.-J.; Shen, Y.-H.; Xie, A.-J.; Yu, S.-H. Nitrogen-doped nanoporous carbon nanosheets derived from plant biomass: an efficient catalyst for oxygen reduction reaction. *Energy Environ. Sci.* **2014**, *7*, 4095−4103.
(46) Liu, G.; Li, X.; Ganesan, P.; Popov, B. N. Studies of oxygen reduction reaction active sites and stability of nitrogen-modified carbon composite catalysts for PEM fuel cells. *Electrochim. Acta* **2010**, *55*, 2853−2858.
(47) Fattah-Alhosseini, A. Passivity of AISI 321 stainless steel in 0.5 M H_2SO_4 solution studied by Mott−Schottky analysis in conjunction with the point defect model. *Arabian J. Chem.* **2016**, *9*, S1342−S1348.
(48) Fernández-Domene, R.; Blasco-Tamarit, E.; García-García, D.; Garcia Antón, J. Passivity breakdown of titanium in LiBr solutions. *J. Electrochem. Soc.* **2014**, *161*, C25−C35.
(49) Choi, C. H.; Lim, H.-K.; Chung, M. W.; Park, J. C.; Shin, H.; Kim, H.; Woo, S. I. Long-range electron transfer over graphene-based catalyst for high-performing oxygen reduction reactions: importance of size, N-doping, and metallic impurities. *J. Am. Chem. Soc.* **2014**, *136*, 9070−9077.
(50) Kim, H.; Lee, K.; Woo, S. I.; Jung, Y. On the mechanism of enhanced oxygen reduction reaction in nitrogen-doped graphene nanoribbons. *Phys. Chem. Chem. Phys.* **2011**, *13*, 17505−17510.
(51) Xiang, Z.; Cao, D.; Huang, L.; Shui, J.; Wang, M.; Dai, L. Nitrogen-Doped Holey Graphitic Carbon from 2D Covalent Organic Polymers for Oxygen Reduction. *Adv. Mater.* **2014**, *26*, 3315−3320.
(52) Wang, M.; Wu, Z.; Dai, L. Graphitic carbon nitrides supported by nitrogen-doped graphene as efficient metal-free electrocatalysts for oxygen reduction. *J. Electroanal. Chem.* **2015**, *753*, 16−20.
(53) Liu, J.; Li, L.; Niu, W.; Wang, N.; Zhao, D.; Zeng, S.; Chen, S. A Hydrogen-Bonded Organic Framework Derived Mesoporous N-doped Carbons for Efficient Electroreduction of Oxygen. *ChemElectroChem* **2016**, *3*, 1116−1123.
(54) Greeley, J.; Stephens, I. E. L.; Bondarenko, A. S.; Johansson, T. P.; Hansen, H. A.; Jaramillo, T. F.; Rossmeisl, J.; Chorkendorff, I.; Norskov, J. K. Alloys of platinum and early transition metals as oxygen reduction electrocatalysts. *Nat. Chem.* **2009**, *1*, 552−556.

DOI: 10.1021/acscatal.8b00338
ACS Catal. 2018, 8, 6827−6836

(55) Jiao, Y.; Zheng, Y.; Jaroniec, M.; Qiao, S. Z. Origin of the Electrocatalytic Oxygen Reduction Activity of Graphene-Based Catalysts: A Roadnnap to Achieve the Best Performance. *J. Am. Chem. Soc.* **2014**, *136*, 4394−4403.
(56) Zhang, J. T.; Zhao, Z. H.; Xia, Z. H.; Dai, L. M. A metal-free bifunctional electrocatalyst for oxygen reduction and oxygen evolution reactions. *Nat. Nanotechnol.* **2015**, *10*, 444−452.
(57) Li, M. T.; Zhang, L. P.; Xu, Q.; Niu, J. B.; Xia, Z. H. N-doped graphene as catalysts for oxygen reduction and oxygen evolution reactions: Theoretical considerations. *J. Catal.* **2014**, *314*, 66−72.
(58) Chai, G. L.; Hou, Z. F.; Shu, D. J.; Ikeda, T.; Terakura, K. Active Sites and Mechanisms for Oxygen Reduction Reaction on Nitrogen-Doped Carbon Alloy Catalysts: Stone-Wales Defect and Curvature Effect. *J. Am. Chem. Soc.* **2014**, *136*, 13629−13640.
(59) Lu, B. Z.; Smart, T. J.; Qin, D. D.; Lu, J. E.; Wang, N.; Chen, L. M.; Peng, Y.; Ping, Y.; Chen, S. W. Nitrogen and Iron-Codoped Carbon Hollow Nanotubules as High-Performance Catalysts toward Oxygen Reduction Reaction: A Combined Experimental and Theoretical Study. *Chem. Mater.* **2017**, *29*, 5617−5628.
(60) Zhang, L. P.; Xia, Z. H. Mechanisms of Oxygen Reduction Reaction on Nitrogen-Doped Graphene for Fuel Cells. *J. Phys. Chem. C* **2011**, *115*, 11170−11176.
(61) Zhao, Z. H.; Xia, Z. H. Design Principles for Dual-Element-Doped Carbon Nanomaterials as Efficient Bifunctional Catalysts for Oxygen Reduction and Evolution Reactions. *ACS Catal.* **2016**, *6*, 1553−1558.
(62) Allen, F. H.; Kennard, O.; Watson, D. G.; Brammer, L.; Orpen, A. G.; Taylor, R. Tables of Bond Lengths Determined by X-ray and Neutron-Diffraction.1. Bond Lengths in Organic-Compounds. *J. Chem. Soc., Perkin Trans. 2* **1987**, *2*, S1−S19.

DOI: 10.1021/acscatal.8b00338
ACS Catal. 2018, 8, 6827−6836

Supporting Information

Graphitic N is Responsible for Oxygen Electroreduction on N-Doped Carbons in Alkaline Electrolytes: Insights from Activity Attenuation Studies and Theoretical Calculations

Nan Wang,[a] Bingzhang Lu,[b] Ligui Li,[a,c,*] Wenhan Niu,[a] Zhenghua Tang,[a,c] Xiongwu Kang,[a] and Shaowei Chen[a,b,*]

[a.] Guangzhou Key Laboratory for Surface Chemistry of Energy Materials, New Energy Research Institute, School of Environment and Energy, South China University of Technology, Guangzhou Higher Education Mega Center, Guangzhou 510006, China. E-mail: esguili@scut.edu.cn (L.G.L.)
[b.] Department of Chemistry and Biochemistry, University of California, 1156 High street, Santa Cruz, California 95064, USA. E-mail: shaowei@ucsc.edu (S.W.C.).
[c.] Guangdong Provincial Key Laboratory of Atmospheric Environment and Pollution Control, School of Environment and Energy, South China University of Technology, Guangzhou 510006, China.

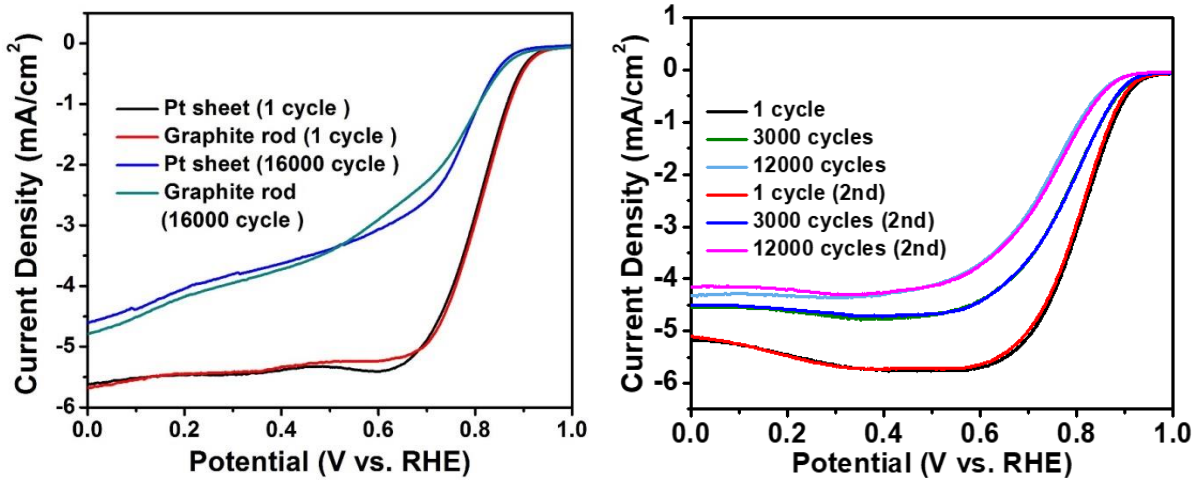

Figure S1. (Left) LSV curves for NGM after 1 and 16000 CV cycles in an O_2-saturated 0.1M KOH aqueous solution using a graphite rod or Pt sheet as the counter electrode. (Right) LSV curves for N-GRW deposited onto two sets of identical RRDEs after 1, 3000 and 12000 CV cycles in an O_2-saturated 0.1M KOH aqueous solution.

We carried out additional experiments by using a graphite rod as the counter electrode. From the LSV curves shown in the left panel of Figure S1, one can see that the ORR performance is almost identical to that using a Pt counter electrode for up to 16000 cycles of potential scans, signifying that the impact from Pt dissolution/deposition, if any, on the ORR performance is negligible.

To test the consistency of the electrodes, the N-GRW catalyst from the same ink was deposited on six RRDEs, which were divided into three groups of two. These three groups then underwent testing for 1, 3000 and 12000 CV cycles, respectively. From the right panel of Figure S1, one can see that the LSV curves for the two electrodes after the same number of CV cycles are almost identical. This

observation highlights the consistency among the electrodes prepared from the same catalyst ink, and hence verify the feasibility of the present methodology in probing the ORR active sites of N-doped carbons by analyzing the attenuation process of the catalytic activity and composition of the catalysts. This is advantageous, as compared to tracking the evolution of the corresponding parameters of a single electrode over time.

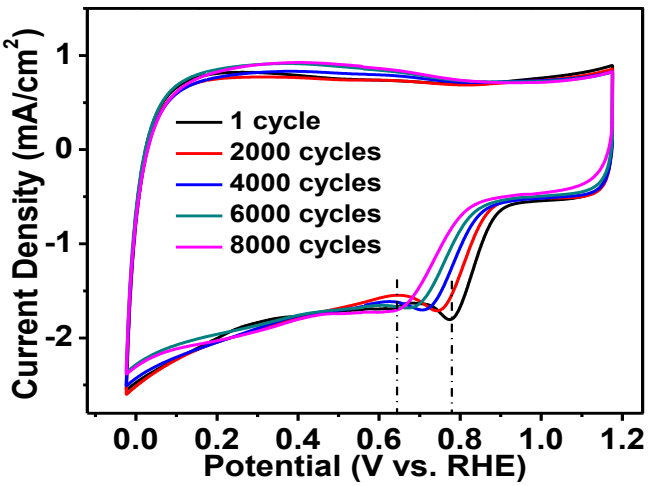

Figure S2. CV curves of N-PC after different potential cycles in an O_2-saturated 0.1M KOH aqueous solution.

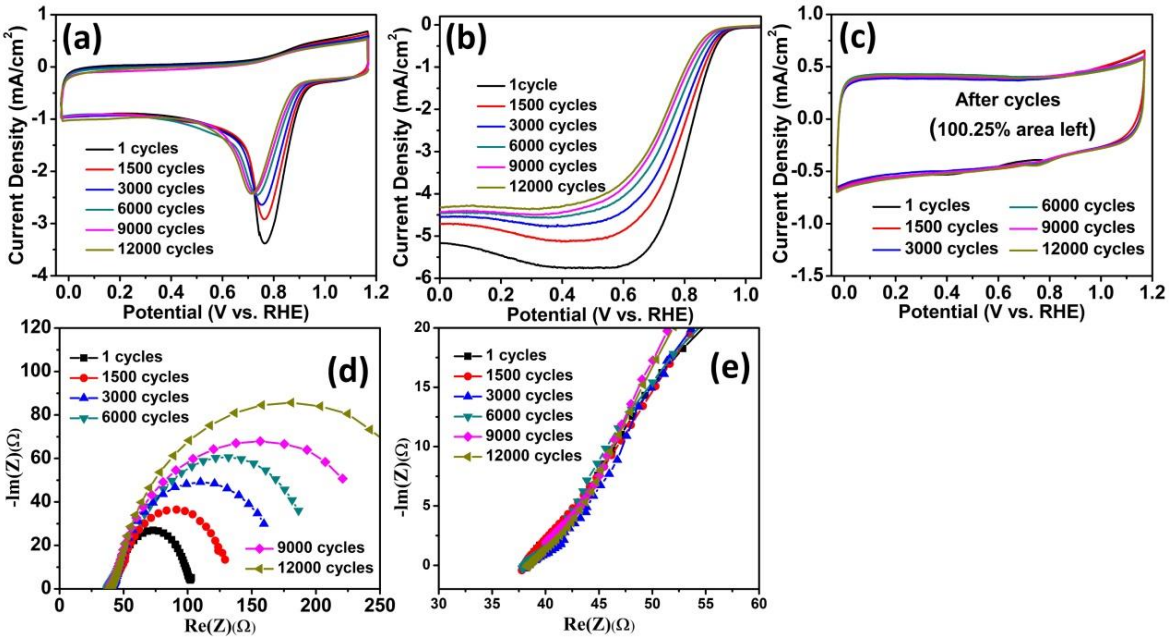

Figure S3. (a) CV and (b) LSV curves of N-GRW in O_2-saturated 0.1 M KOH. (c) CV curves in N_2-saturated 0.1 M KOH. EIS curves in the (d) low-frequency and (e) high-frequency region. Experimental conditions are the same as those in Figure 2.

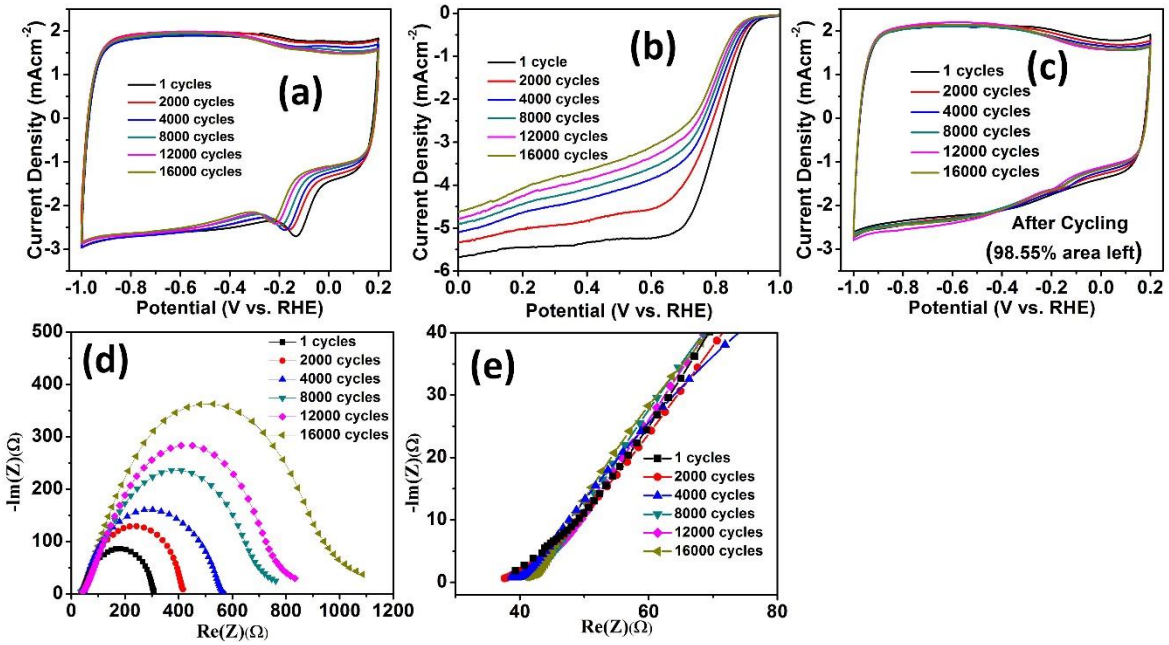

Figure S4. (a) CV curves and (b) LSV curves of NGM in O_2-saturated 0.1 M KOH. (c) CV curves in N_2-saturated 0.1 M KOH. EIS curves in the (d) low-frequency and (e) high-frequency region. Experimental conditions are the same as those in Figure 2.

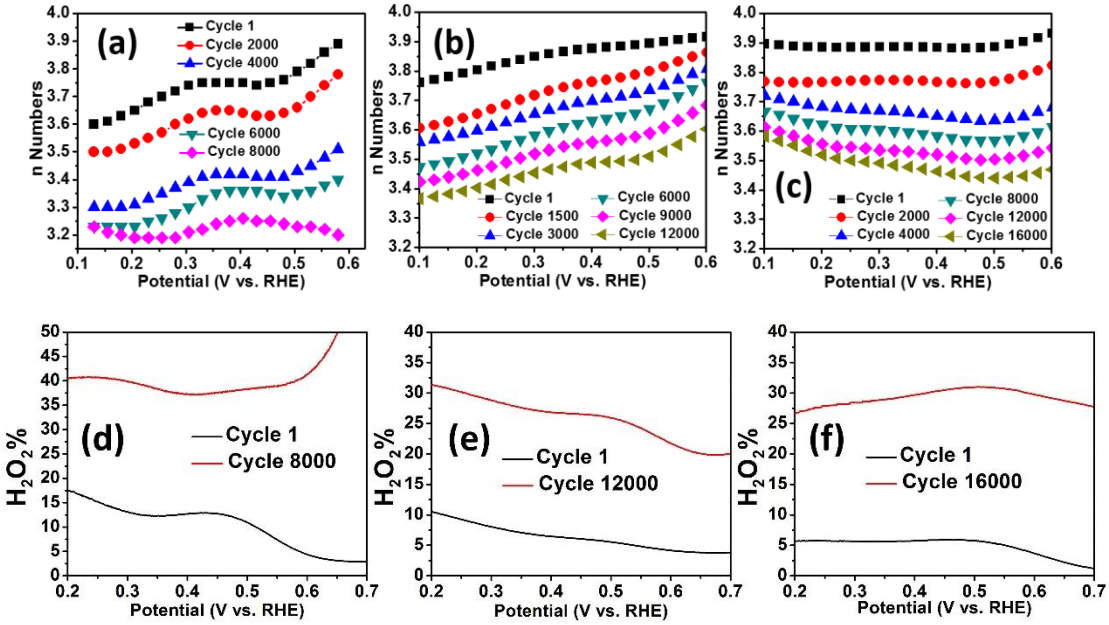

Figure S5. (a-c) Number of electron transfer (n) and the corresponding (d-f) H_2O_2 yield for (a, d) N-PC, (b, e) N-GRW and (c, f) NGM after different numbers of potential cycles.

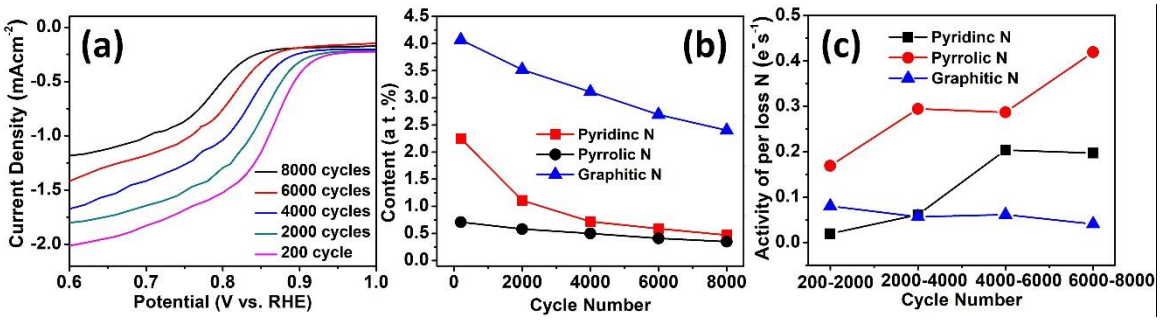

Figure S6. (a) Polarization curves of N-PC on a non-rotating glassy carbon electrode (area 0.07 cm^2) after different CV cycles in O_2-saturated 0.1M KOH aqueous solution at the sweep rate of 10 mVs^{-1} and a catalyst loading of 0.142 mg cm^{-2}; (b) The corresponding content of three typical N doping configurations after various potential cycles. (c) Plots of the specific activity per pyridinic N, pyrrolic N and graphitic N atom in the N-PC catalyst vs. cycle number.

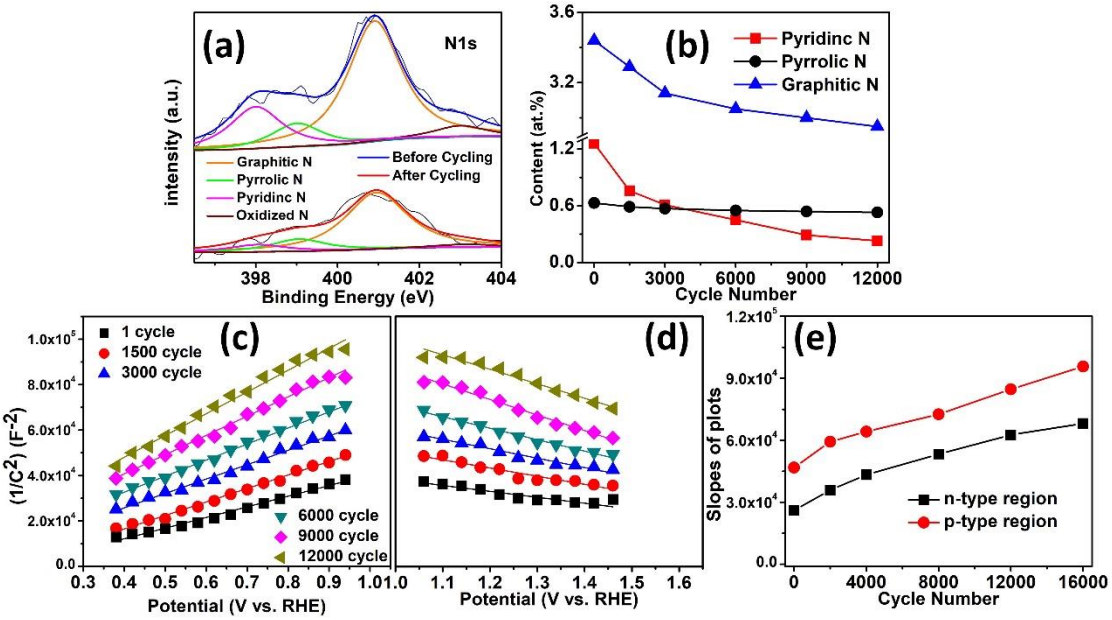

Figure S7. (a) High-resolution N 1s scans of N-GRW before and after prolonged cycling. (b) Diminishing trend of the three nitrogen doping configurations in the catalyst. Mott-Schottky analysis conducted at the frequency of 100 Hz in Ar-saturated 0.1 M KOH with the catalyst loading of 102 μg cm^{-2} on a glassy carbon electrode. The plots of C_{SCL}^{-2} vs. potential *E* show positive (c) and negative (d) slopes for the N-doped carbon sample after different number of potential cycles. (e) Plots of absolute slopes observed in (c) and (d) against cycling number.

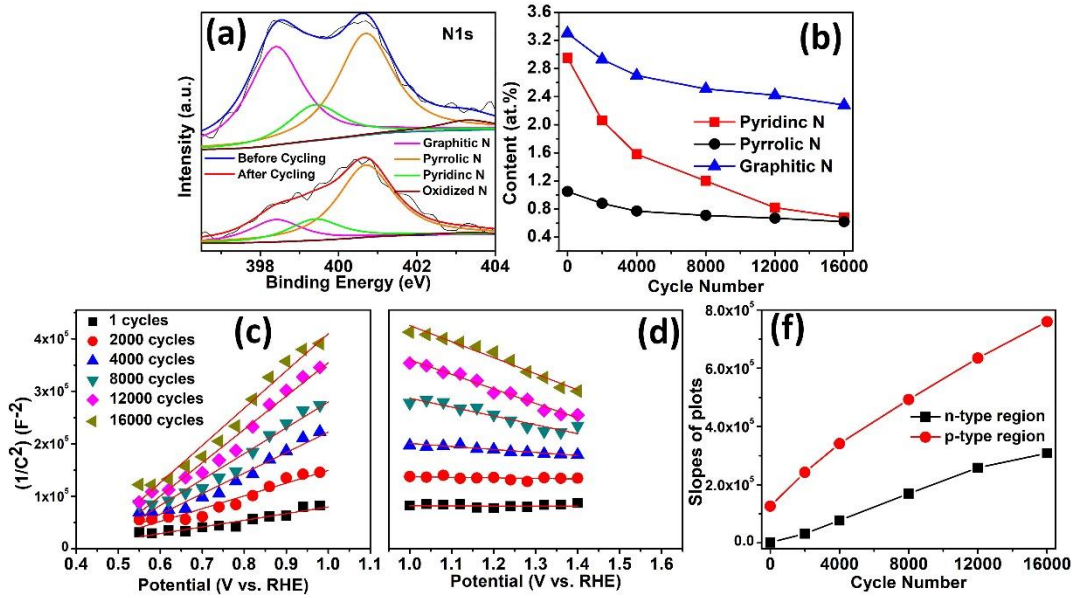

Figure S8. (a) High-resolution N 1s spectra of NGM before and after cycling tests. (b) Diminishing trend of the three nitrogen doping configurations in the catalyst. Mott-Schottky analysis conducted at the frequency of 100 Hz in Ar-saturated 0.1 M KOH with a catalyst loading of 102 μg cm^{-2} on a glassy carbon electrode. The plots of C_{SCL}^{-2} vs. potential *E* show positive (c) and negative (d) slopes for the N-doped carbon sample after different number of potential cycles. (e) Plots of absolute slopes observed in (c) and (d) against cycling number.

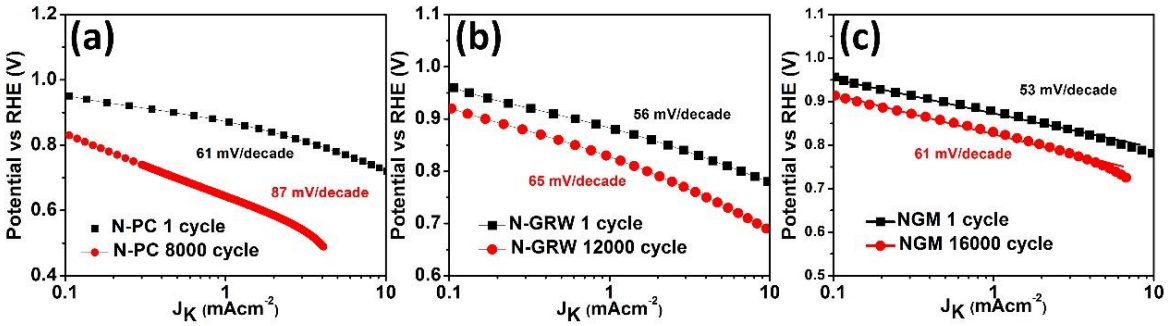

Figure S9. Tafel plots of the N-doped carbon samples before and after long-term cycling: (a) N-PC, (b) N-GRW, and (c) NGM.

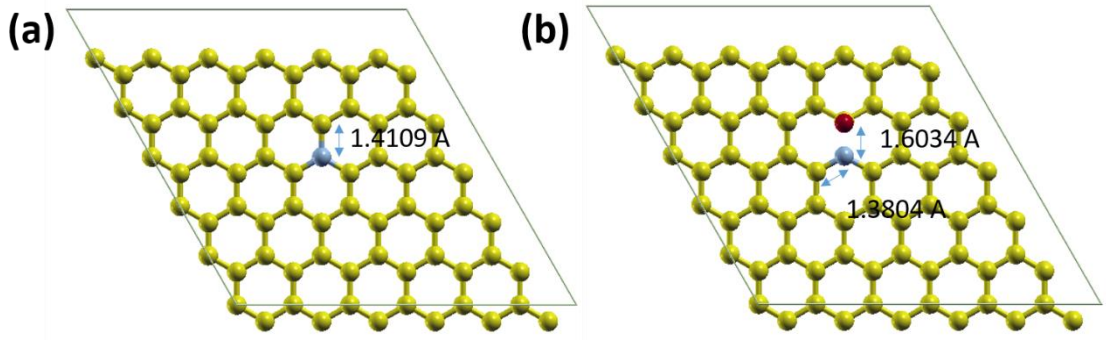

Figure S10. Change of graphitic C-N bond length (a) before and (b) after the adsorption of O* oxygen intermediates.

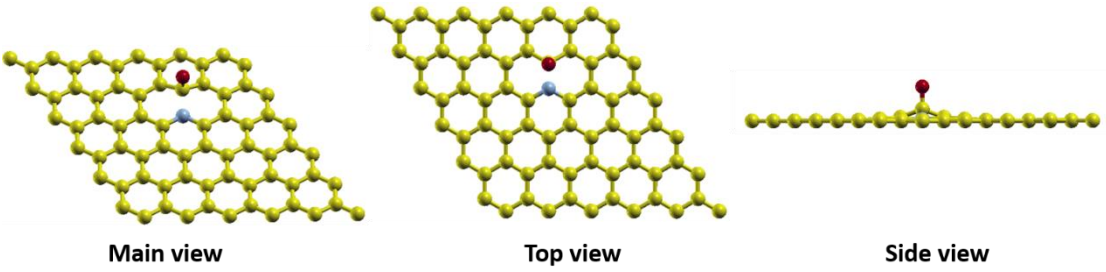

Figure S11. Breaking of graphitic C-N bond after oxygen adsorption in three different viewing angles.